Article:
Dong, B., Hull, S. and West, A.R. orcid.org/0000-0002-5492-2102 (2018) Phase formation, crystallography and ionic conductivity of lithium manganese orthosilicates. Inorganic Chemistry. ISSN 0020-1669

https://doi.org/10.1021/acs.inorgchem.8b02894

Phase formation, crystallography and ionic conductivity of LiMn orthosilicates

Bo Dong[†,‡], *Stephen Hull*[‡], *Anthony R. West*[†]

†University of Sheffield, Department of Material Science and Engineering, Mappin Street, Sheffield S1 3JD, UK

‡The ISIS Facility, STFC Rutherford-Appleton Laboratory, Didcot, Oxfordshire OX11 0QX, UK

ABSTRACT: On the orthosilicate join, Li_4SiO_4-Mn_2SiO_4, the new phase $Li_3Mn_{0.5}SiO_4$ and a range of $Li_{2+2x}Mn_{1-x}SiO_4$ solid solutions with ~0.76 ≤x ≤1 have been prepared and characterised. $Li_3Mn_{0.5}SiO_4$ is orthorhombic, space group *Pnma*, with *a* = 10.722(3)Å, *b* = 6.239(2)Å, *c* = 5.052(3)Å. Combined analysis of X-ray and neutron powder diffraction data show that its structure is derived from the γ_{II} tetrahedral structural family typified by Li_3PO_4, but with additional Li^+ in partially-occupied, distorted octahedral sites. These octahedral sites are linked by a combination of edge- and face-sharing, similar to that in the nickel arsenide structure and their partial occupancy is responsible for an Li^+ ion conductivity of eg ~ $1x10^{-8}$ Scm^{-1} at 60 °C, with activation energy 0.93(1) eV, which is many orders of magnitude higher than that of Li_2MnSiO_4.

Introduction

Orthosilicates with the general formula Li_2MSiO_4 (M = Fe, Mn, Co) have been proposed as possible cathodes for lithium ion batteries due to their high theoretical capacity (333 mAh/g), based on the assumption that two Li^+ ions can be (de)intercalated per formula unit during charge/discharge reactions[1-5]. Computational modelling showed that the theoretical voltages for the Mn^{2+}/Mn^{3+} and Mn^{3+}/Mn^{4+} redox steps are in the range from 4.1 to 4.5 V, which is favourable for high energy cathode materials, whilst those of Fe^{3+}/Fe^{4+} and Co^{3+}/Co^{4+}, 4.8 to 5 V, are outside the voltage stability window of usual liquid electrolytes[6].

Li_2MnSiO_4 shows four main polymorphs, characterised by different distributions and orientations of LiO_4, MnO_4 and SiO_4 tetrahedra. These polymorphs are orthorhombic, in space groups $Pmn2_1$ and $Pmnb$, and monoclinic, in space groups $P2_1/n$ and Pn [7]. Crystallographic studies are reviewed in the Supporting Information of reference [8], which also includes comments on possible inaccuracies in partial site occupancies in structural reports based on powder diffraction data. Information on the polymorphism, crystal structures and electrochemical performance of the Mn, Fe and Co analogues are highlighted in reference [9]. The four polymorphs of Li_2MnSiO_4 are all related to the β and γ families of so-called tetrahedral structures based on Li_3PO_4 and are given a notation based on isostructural Li_2ZnSiO_4 phases [10,11], though there appear to be some inconsistencies in the literature over polymorph labelling. In these structures, Li,

Mn and Si cations are distributed over various tetrahedral sites within a distorted hexagonal close-packed, *hcp*, oxygen array. The key features of the four structures are illustrated in figure 1 [8, 12-14].

The $Pmn2_1$ and *Pn* polymorphs are structurally-related to β Li_3PO_4, in which all the tetrahedra point in the same direction. They may be described as cation-ordered wurtzite superstructures with different ordering arrangements and an *hcp* oxygen sublattice. In the $Pmn2_1$ form, isostructural with β Li_3PO_4 and given the notation β_{II} Li_2MnSiO_4, chains of LiO_4 tetrahedra run parallel to the *a*-axis together with chains of alternating SiO_4 and MnO_4 tetrahedra. In the metastable *Pn* form, prepared by ion-exchange of Na_2MnSiO_4 at 300 ºC [12], chains of alternating LiO_4 and MnO_4 tetrahedra run parallel to chains of alternating SiO_4 and MnO_4 tetrahedra. Both of these structures have 3-dimensional frameworks built of corner-sharing tetrahedra in which each corner is shared between four tetrahedra. Within this framework, empty tetrahedral and octahedral sites are also present.

The *Pmnb* and $P2_1/n$ structures are related to γ Li_3PO_4 and contain tetrahedra that point 'up' and 'down' in two orientations. The effect of this is to create pairs of edge-sharing tetrahedra which link through their corners to form a 3-dimensional framework. In the $P2_1/n$ form, pairs of LiO_4/MnO_4 and LiO_4/LiO_4 tetrahedra share edges, whilst the *Pmnb* variant contains groups of three, LiO_4–LiO_4–MnO_4, edge-sharing tetrahedra [9].

Li_2MnSiO_4 with the $Pmn2_1$ structure was prepared by Dominko *et al*. by a sol-gel method [1], whilst Politaev *et al*. reported the monoclinic $P2_1/n$ polymorph prepared by solid state reaction in H_2 at 950-1150 ºC [13]. A phase transition of Li_2MnSiO_4 from the β to the γ polymorph occurs at around 750 ºC [15]. The electrochemical performance of $Pmn2_1$ Li_2MnSiO_4/C composites is reported to be much better than that of the $P2_1/n$ phase and is attributed to differences in activation energies and hopping distances [16]. Many studies have been reported with the objective of improving the electrochemical performance of Li_2MnSiO_4 as a potential cathode material for battery applications. It has a low electronic conductivity (about 10^{-16} S/cm at room temperature), but carbon coating [17], reduction in particle size [18] and doping [19] have all been used to enhance its physical and/or chemical properties, increase the conductivity and prolong cycle life.

The crystal structure of low Li_4SiO_4 has a large monoclinic unit cell (a = 11.54Å, b = 6.09Å, c = 16.65Å, β = 99.5º), with Li located in a number of crystallographically distinct sites that have coordination numbers of 4, 5 and 6 [20]. Much of the early work on Li_4SiO_4 and its solid solutions was based on a subcell (a = 5.14Å, b = 6.10Å, c = 5.30Å, β = 90.5º), since the superlattice peaks were too small to detect. On heating, Li_4SiO_4 undergoes a complex sequence of transitions over the temperature range 600 to 750 ºC [21]. Structural information on the intermediate phases and the high temperature form above 750 ºC is not available, although there are many similarities between their X-ray diffraction data, indicating a strong structural similarity.

In orthosilicate systems, tetrahedral-structure phases of general formula Li_2MSiO_4 form with *M*=Zn, Mg, Co, Mn and Fe [10,11]. The Zn and Mg systems also show extensive solid solution formation and composition-dependent polymorphism on the joins Li_4SiO_4-M_2SiO_4 [21,22]. A limited solid solution range was reported for *M*=Mn [13]. In a more recent study [23], although non-stoichiometric compositions on the orthosilicate join were not studied directly, Rietveld refinement of XRD data of phase mixtures indicated the presence of an Li-rich composition with a structure derived from that of Li_2MnSiO_4. Analogous compositions in the germanate systems have been widely studied and Li-rich compositions with *M*=Zn have exceptionally high Li^+ ion conductivity. Indeed, their discovery triggered interest in the so-called LISICON materials [24]. One objective of the present work is to survey similar compositions on the orthosilicate join with *M*=Mn to seek possible new phases and measure their properties. Here we report the formation of new solid solutions based on Li_4SiO_4 and a new, Li-rich, ionically-conducting phase, $Li_3Mn_{0.5}SiO_4$ with a γ-related structure.

Experimental

Manganese(II) oxide (Sigma-Aldrich, 99%), lithium carbonate (Sigma-Aldrich, 99%) and silica (Alfa Aesar, 99.5%) were dried at 180 ºC and used as reagents. Samples with composition $Li_{2+2x}Mn_{1-x}SiO_4$ between Li_4SiO_4(L_2S) and Mn_2SiO_4(M_2S) were prepared in two stages (using the abbreviations such as L_2S and M_2S in which *L*, *M* and *S* refer to the oxides Li_2O, MnO and SiO_2, respectively). First, the end-members were prepared by reaction in Au boats at 800 ºC for 12 h in air (L_2S)

and in Pt boats at 1200 °C for 20 h in N_2 (M_2S). Second, mixtures of L_2S and M_2S in different ratios were reacted in Au boats at 800 °C in an atmosphere of 5% H_2 in N_2 for 10 h. Small samples of each composition were subsequently heated in Pt envelopes at 1000 °C in N_2 for 30 min and then quenched into liquid N_2.

A Stoe STADI P X-ray diffractometer with Mo $K\alpha_1$ (λ= 0.70926 Å) radiation and a linear position sensitive detector (PSD) was used to collect powder X-ray diffraction (XRD) data for phase analysis and lattice parameter calculation; Mo radiation was used instead of Cu to avoid problems with background fluorescence. Patterns were recorded over the range $5 \leq 2\theta(^{o}) \leq 40$, which covers a *d*-spacing range of $1.04 \leq d(\text{Å}) \leq 8.14$ (although data were collected over a limited 2θ range only, large datasets were obtained because of the short wavelength of the Mo radiation). The neutron powder diffraction (NPD) measurements were performed using the GEM diffractometer at the ISIS Facility, Rutherford Appleton Laboratory, United Kingdom [25]. Data were collected using the detector bank covering the scattering angles $79 \leq 2\theta(^{o}) \leq 106$ (chosen as it provides the most suitable *d*-spacing range and $\Delta d/d$ resolution) and over the time-of-flight range $3.0 \leq t(\text{msec}) \leq 19.5$. The latter corresponds to a *d*-spacing range of $0.45 \leq d(\text{Å}) \leq 2.92$; it is important to note that the NPD data retained good resolution at low d-spacings, which is essential to minimise correlations between thermal vibration parameters and fractional site occupancies. The powdered sample was encapsulated in a cylindrical, 11 mm diameter, vanadium can and measured for approximately 2 h. Rietveld refinement of the XRD and NPD data used the EXPGUI interface of the GSAS suite of programs [26].

For electrical property measurements, pellets of $Li_{2+2x}Mn_{1-x}SiO_4$ were sintered at 800 to 1000 ºC for 4 h in an H_2/N_2 atmosphere. Electrodes of either sputtered Au or Au paste were fabricated on opposite pellet faces. Pellets with electrodes attached were placed in an in-house built conductivity jig inside a horizontal tube furnace and measurements recorded in N_2. Impedance data were collected using a Solartron 1260 with a voltage of 100 mV ac and a sweep frequency range from 10^{-2} to 10^6 Hz.

Results and Discussion

Compound and solid solution formation

Results are presented using the general formula $Li_{2+2x}Mn_{1-x}SiO_4$. Composition x = 0, Li_2MnSiO_4 (*LMS*) is already well-established in the literature, as are the end-member phases, x = 1 (L_2S) and x = -1, (M_2S). XRD results for samples heated at 800 ºC, followed by programmed cool at 5 ºC/min are shown in figure 2 and for samples quenched from 1000 ºC in figure 3. From these results, several new, single phase compositions were established and are summarized in table 1.

At the composition x = 0.5, a new phase, $Li_3Mn_{0.5}SiO_4$ (L_3MS_2) was prepared. XRD data for L_3MS_2 were successfully indexed using an orthorhombic unit cell of dimensions a = 10.722(3) Å, b = 6.239(2) Å and c = 5.052(3)Å, whose systematic absence conditions on reflections were consistent with space group *Pnma* (see table 2). These assignments indicate a strong similarity to the γ tetrahedral structures, such as Li_3PO_4 and the LISICON solid solutions. However, unlike the Zn-based LISICON solid solutions that have been reported [21,27] and which have variable composition,

L_3MS_2 appears to be either a line phase or a phase of limited compositional extent since samples of x=0.4 and 0.6 both contained significant amounts of second phases in addition to L_3MS_2 as the main phase. L_3MS_2 was prepared in N_2 to control the oxidation state of Mn as 2+ and is stable to at least 1000 ºC. On heating in air, however, its colour changed from dark grey to orange and extra lines appeared in the powder XRD pattern; these were not characterized further. Oxidation appeared to have occurred, therefore, but could be reversed by reheating samples in N_2/H_2 at 800 ºC.

L_2S forms an extensive range of solid solution over the range $1 \geq x > 0.7$, with two polymorphic forms. The high temperature form observed within the samples quenched from 1000 ºC, figure 3, has a very similar powder XRD pattern to stoichiometric L_2S. Data for x = 0.7 are listed in table 3 and were indexed on a similar monoclinic subcell to that reported earlier for L_2S, as referred to above. The variation with composition of the lattice parameters of the solid solution (referred to as L_2S *ss*) quenched from 1000 ºC is shown in figure 4, showing that the unit cell volume decreases with increasing x whilst the *b* lattice parameter increases. Although the number of data points is small, the solid solution limit at 1000 ºC is estimated to be 0.76(2), consistent with the phase analysis results reported in table 1. We have not made any attempt to determine whether the solid solution limits of any of the phases show significant temperature-dependence, other than noting the observation that the compositional limits of single phase samples that were either slow-cooled from 800 ºC or quenched from 1000 ºC, were similar.

As shown in figure 2, the low temperature form of L_2S *ss* has extra XRD lines and appears to be a superstructure derived from L_2S. The intensities of the extra lines increase with decreasing x and, again, the solid solution limit is approximately x = 0.75. Further characterization of low L_2S *ss* has not been carried out, but we note the similarity of the XRD data and the extra lines to data obtained for analogous Zn-based L_2S solid solutions [21].

Two forms of *LMS* were encountered, the β form (space group $Pmn2_1$) in the sample slow-cooled from 800 ºC and the γ form (space group $P2_1/n$) quenched from 1000 ºC. In Li-rich compositions, the polymorph obtained appeared to change and the *Pmnb* variant was observed in a slow cooled sample of x = 0.1. The γ form appears to form little or no solid solution with varying x (see table 1), since phase mixtures were observed in samples quenched from 1000 ºC. From the literature on *LMS* and its polymorphism [13], it has been reported that a solid solution forms over the range 0.2>x>-0.2.

Rietveld refinement of the XRD and NPD data for $Li_3Mn_{0.5}SiO_4$

The unit cell dimensions and space group of L_3MS_2 determined from the XRD data (table 2) strongly suggest that its structure is LISICON-related. As a consequence, the starting model chosen for refinement of the XRD and NPD data was based on that of γ Li_3PO_4, with the positional coordinates for the Si and O taken from those reported for Ge and O, respectively, in $Li_3Zn_{0.5}GeO_4$ [28]. With the initial assumption that the Li and Mn occupy tetrahedrally co-ordinated sites within the anion sublattice, there are a

total of 32 such positions within the unit cell, generated by 6 symmetry-independent sites: 4 sets of 4-fold sites at x,$^1/_4$,z, *etc*. (one of which is occupied by Si) and 2 sets of 8-fold general positions at x,y,z, *etc*. To determine the distribution of the Li and Mn cations over the available tetrahedral sites, preliminary refinements were performed using the NPD and XRD data separately. In the former case, the relative coherent neutron scattering lengths of the atomic species [29] provided a good sensitivity to the locations of the Li/Mn cations, but did not distinguish between these two species well. In the latter case, the XRD method was highly complementary and significantly more sensitive to the location of Mn than of Li.

The process described above provided a starting model in which the Li and Mn appeared to be disordered over two tetrahedral sites, one 8-fold position labelled Li1/Mn1 and a 4-fold position labelled Li2/Mn2. Simultaneous refinement of both XRD and NPD datasets was then used, with the two backgrounds (coefficients of a 10th order shifted Chebyschev polynomial), two scale factors, the lattice parameters and two sets of peak shape parameters refined in sequence. This was followed by allowing the positional parameters and then the isotropic thermal vibration parameters to vary, which resulted in reasonable agreement between the measured and calculated diffraction patterns for both radiations. Finally, the two ratios of Li and Mn on the two tetrahedral positions were varied, subject to the constraint that both sites remained fully occupied. At this stage, the quality-of-fit parameter, χ^2, had a value of 5.01 and the chemical formula corresponded to $Li_{2.57(9)}Mn_{0.43(5)}SiO_4$.

To identify any additional lattice sites that might contain Li and/or Mn, a Fourier difference map was constructed using the NPD data. Significant scattering was observed at two 4-fold sites, with fractional co-ordinates around 0.21,$^1/_4$,-0.05, *etc*. and $^1/_2$,0,0, *etc*. These are essentially octahedrally co-ordinated positions, though the former is somewhat displaced from the centre of the octahedron. Trial refinements of partial occupancies of these new sites using the XRD data alone, and with all other parameters fixed, indicated that both these sites were partially occupied by Li at the level of around 0.2. This was subsequently confirmed by simultaneous refinement of the XRD and NPD data, with the two new sites labelled Li3 and Li4, respectively. Final fits varying all parameters, including the positional, isotropic thermal vibration and occupancy parameters of the Li3 and Li4 sites, gave an excellent fit to both diffraction datasets, with the experimental, calculated and difference profiles shown in figure 5, the values given in table 4 and a goodness-of-fit χ^2=4.68. Derived bond lengths are summarised in table 5 and bond angles for the cation-centred polyhedra are given in table 6. The composition obtained from these refinements, $Li_{2.86(0.09)}Mn_{0.46(0.03)}SiO_4$, is within two estimated standard deviations of the expected composition of L_3MS_2.

Crystal structure of $Li_3Mn_{0.5}SiO_4$

The crystal structure of L_3MS_2 is related to that of other Li-rich LISICONs and can be regarded as an orthorhombic, γ_{II} derivative structure. The arrangement of the anion sublattice is close to *hcp*, with a shift of the O2 oxide ions by ~0.5Å broadly along the

c-axis and displacements of the O1 and O3 ions away from their ideal positions by ~0.3Å principally within the *ab* plane. The positional parameters for the corresponding *hcp*-based structure are included in table 4.

The distortions of the *hcp* anion sublattice result in one of the 4-fold sets of tetrahedra becoming slightly smaller, and these are occupied by the Si cations (see table 5). The remaining tetrahedra also become distorted, as shown in figures 6(*a*) and 6(*b*). The arrangement of the tetrahedra occupied by Li1/Mn1, Li2/Mn2 and Si is shown in figure 5, with their bases forming the *cp* oxide layers perpendicular to *c*, but with a mixture of two orientations, pointing either 'up' and 'down' the *c*-axis, T_+ and T_- (see figure 7(*a*)). This corresponds to the polyhedral arrangement of a γ tetrahedral structure, such as γ-Li_3PO_4. The SiO_4 tetrahedra share only their corners with $(Li/Mn)O_4$ tetrahedra, whereas edge-sharing occurs between the $(Li/Mn)O_4$ tetrahedra.

A projection of the structure down the [001] axis is shown in figure 7(*b*), with half the unit cell contents in the *c* direction of several unit cells shown. Two adjacent distorted *hcp* oxide layers are shown as black and red spheres. Between the oxide layers, tetrahedral sites in both T_+ and T_- orientations can be seen but, overall, only half the available tetrahedral sites, both T_+ and T_-, are occupied, in an ordered fashion. There are different ways to view the ordering; for instance, as rows of corner-sharing tetrahedral sites, either T_+ or T_-, which run parallel to [110], such that adjacent rows alternate between having sequences of three occupied - one empty sites and three

empty – one occupied sites. Alternatively, parallel to [010], there are infinite double chains of edge-sharing $(Li/Mn)O_4$ tetrahedra in which all T_+ and T_- sites are occupied.

Thus far, the structure of L_3MS_2 is very similar to that of γ Li_3PO_4 and the *Pmnb*-structured polymorph of Li_2MnSiO_4. However, additional Li3 and Li4 occupy partially some distorted octahedral sites, shown as blue and yellow spheres in figure 7, which are empty in γ-Li_3PO_4. The octahedral sites in the *hcp* array have the same distribution as the octahedral sites in the NiAs structure, where adjacent sites share faces in the *c* direction and edges in the *ab* plane. In L_3MS_2, only half the octahedral are occupied, partially, but in an ordered way by Li^+. The combined occupancy of the octahedral sites is, however, only a small fraction, around 8%, of all the available octahedral sites.

The only other structural report of a Li-rich LISICON phase is for compositions, $Li_{2+2x}Zn_{1-x}GeO_4$ [28]. For the specific composition x = 0.5, the Li1/Zn1 site is, similarly, fully occupied by a mixture of Li and Zn. The Li2/Zn2 site distribution is more complex, however, and full occupancy is achieved by partial occupancy of an additional, face-sharing Li2*a* site. The grossly-distorted Li3 octahedral site is partially occupied by Li in both structures but with rather different *z* coordinates. A major difference from the present structure is that $Li_{2+2x}Zn_{1-x}GeO_4$ forms a very extensive solid solution over the range $-0.36<x<0.87$ [27] and, therefore, a continuous variation of some site occupancies with composition is expected. Partial occupancies of the Li4

sites were reported in $Li_{3.5}Zn_{0.25}GeO_4$, as well as in L_3MS_2, but this site appears to be empty in the analogous Zn composition, $Li_3Zn_{0.5}GeO_4$.

Electrical property measurements

Impedance data of a sintered pellet of L_3MS_2 are shown in figure 8 and indicate two main components in the impedance Z* response, see figure 8(*a*). The high frequency arc is attributed to the sample bulk, as shown by overlapping peaks at high frequency in the combined M''/Z'' spectra (figure 8(*d*)). The low frequency inclined spike is attributed to a capacitive impedance at the sample-electrode interface, as shown by capacitance data in figure 8(*b*), which reach values as high as 30 μFcm^{-1} at 0.01 Hz and 164 ^oC; this indicates that conduction is predominantly ionic. From the low frequency intercept of the impedance arc on the Z' axis, values of the sample resistance were obtained and are shown in Arrhenius format in figure 9(*a*). The data may show slight curvature, but to a first approximation, are essentially linear with an activation energy of 0.93(1) eV. The conductivity of L_3MS_2 is attributed to Li^+ ions, therefore, and is many orders of magnitude higher than that of *LMS* (space group $Pmn2_1$), shown also in figure 9(*b*). Depending on temperature, the conductivity of L_3MS_2 is also 1-2 orders of magnitude higher than that of L_2S. Impedance data of *LMS* (not shown), contained no evidence of a low frequency, high capacitance electrode spike and its very low conductivity is, therefore, probably electronic in origin.

The Li^+ ion conductivity of L_3MS_2 appears to be related directly to the partially-occupied octahedral sites since, in the *Pmnb* polymorph of *LMS*, the

octahedral sites are empty and the phase is an electrical insulator, both ionic and electronic. Only ~8% of the octahedral sites are effectively occupied in L_3MS_2, but this is made up of partial occupancy of half of all of the available octahedral sites. The structure therefore has a NiAs-like network of face- and edge-sharing octahedral sites whose partial occupancy and ready site exchange accounts for the high level of Li^+ ion conductivity.

Impedance data of high L_2S *ss* (not shown) were similar in general appearance to those of L_3MS_2; a low frequency inclined spike with capacitance values at low frequency of >1 μFcm^{-1} indicated that these materials are also ionic conductors and therefore that Li^+ ions are the likely charge carrier. Arrhenius plots of L_2S and the high and low forms of L_2S *ss* with x = 0.75, are shown in figure 9(*b*). The conductivity of the high form of L_2S *ss* is slightly higher than that of L_2S and approximately one order of magnitude higher than that of low L_2S *ss*. The superstructure XRD peaks observed in low L_2S *ss* are probably a consequence of ordering within the crystal structure and trapping of some of the mobile Li^+ ions and is responsible for the reduction in conductivity.

Conclusions

$Li_3Mn_{0.5}SiO_4$ was readily prepared by solid state reaction in an inert atmosphere to prevent oxidation of Mn^{2+}. $Li_3Mn_{0.5}SiO_4$ is a new member of the family of γ tetrahedral structures. It has a distorted *hcp* oxide array with half of both T_+ and T_- tetrahedral sites occupied by either Si or a disordered mixture of Li and Mn; in this

sense, the structure is similar to that of γ Li_3PO_4 and the *Pmnb* polymorph of Li_2MnSiO_4. In addition, however, $^1/_2$ of the octahedral sites are occupied partially by Li^+ to give, unusually, a stoichiometric phase that has a great deal of cation disorder.

The octahedral sites link by either face-sharing or edge-sharing and this provides a 3D conduction pathway for the mobile Li^+ ions. Impedance data recorded at low frequencies show capacitance values as high as 30 μFcm^{-1}, which is a very strong indicator that conduction is ionic and leads to a blocking double layer capacitance at the sample-electrode interfaces. The defect and disordered nature of the crystal structure, with partial occupancy of Li^+ ions on the octahedral sites, confirms that the ionically-conducting species are, indeed, Li^+ ions. There was no evidence of any residual electronic conductivity since, if present, this would have caused a collapse of the low frequency impedance spike due to the presence of an alternative electronic pathway in parallel with the blocking double layer capacitance. This is also consistent with the expectation that the charge state on Mn in $Li_3Mn_{0.5}SiO_4$, that was prepared at high temperatures in an inert atmosphere, was exclusively Mn^{2+}.

The activation energy for Li^+ conduction in $Li_3Mn_{0.5}SiO_4$ is 0.93 eV, which is significantly higher than that of the very best Li^+ ion conductors,~ 0.3-0.4 eV, and indeed, is higher than that of undoped Li_4SiO_4, Fig 9(a), although this has a lower overall conductivity. The activation energy for conduction in $Li_3Mn_{0.5}SiO_4$ appears to contain a significant carrier creation component as shown by the value of ~10^5 for the pre-exponential factor, A, in the Arrhenius equation $\sigma = A \exp(-E/kT)$ that was used

to fit the conductivity data. For ionic conductors without a carrier creation component in the activation energy, an A value in the range 10-100 is more usual. This means, therefore, that the defect structure of $Li_3Mn_{0.5}SiO_4$ is temperature-dependent and additional mobile carriers are created with increasing temperature. A corollary to this observation is that the dynamic disorder in $Li_3Mn_{0.5}SiO_4$ increases with temperature and therefore, if this state could be preserved to lower temperatures by some means, then significantly higher ionic conductivities may be possible.

There are considerable similarities, and differences, in the existence of phases and solid solutions between the related orthosilicate systems with *M*=Zn and Mg and the Mn-based system studied here. A similar $Li_3Mn_{0.5}SiO_4$ line phase does not exist in the Mg system, but is present simply as one composition in a wide range of γ_{II} solid solutions in the Zn silicate and germanate systems. A range of M^{2+} solid solutions based on the Li_4SiO_4 end-member forms in the Mn system and is commonly found with other divalent M^{2+} dopants. These are also Li^+ ion conductors, but not as good as the non-stoichiometric γ materials such as L_3MS_2 and LISICON materials. A recent report of an Li-rich, Fe-containing solid solution is given in [30]

Notes

The authors declare no competing financial interest.

Present Address

Bo Dong, School of Chemistry, University of Birmingham, B15 2TT, UK.

Acknowledgements

B.D. thanks STFC and EPSRC for a Global Challenge PhD studentship, STFC for allocation of the neutron beam time and R.I. Smith for assistance with the neutron data collection.

References

1 Dominko, R.; Bele, M.; Gaberšček, M.; Meden, A.; Remškar, M.; Jamnik, J. Structure and electrochemical performance of Li_2MnSiO_4 and Li_2FeSiO_4 as potential Li-battery cathode materials. Electrochemistry Communications, (2006), 8, 217.

2 Dominko, R. Li_2MSiO_4 (M=Fe and/or Mn) cathode materials. Journal of Power Sources, (2008), 184, 462.

3 Kokalj, A.; Dominko, R.; Mali, G.; Meden, A.; Gaberscek, M.; Jamnik, J. Beyond One-Electron Reaction in Li Cathode Materials: Designing $Li_2Mn_xFe_{1-x}SiO_4$. Chemistry of Materials, (2007), 19, 3633.

4 Nyten A.; Abouimrane A.; Armand M.; Gustafsson, T.; Thomas J.O. Electrochemical performance of Li_2FeSiO_4 as a new Li-battery cathode material. Electrochemistry Communications, (2005), 7, 156.

5 Arroyo-de Dompablo, M. E.; Armand, M.; Tarascon, J. M.; Amador, U. On-demand design of polyoxianionic cathode materials based on electronegativity correlations: An exploration of the Li_2MSiO_4 system (M=Fe, Mn, Co, Ni). Electrochemistry Communications, (2006), 8, 1292.

6 Saracibar, A.; Van der Ven, A.; Arroyo-de Dompablo, M. E. Crystal structure, energetics, and electrochemistry of Li_2FeSiO_4 polymorphs from first principles Calculations. Chemistry of Materials, (2012), 24, 495.

7 Gummow, R. J.; He, Y. Recent progress in the development of Li_2MnSiO_4 cathode materials. Journal of Power Sources, (2014), 253, 315.

8 Sato M.; Ishigaki T.; Uematsu K.; Toda K.; Okawa H. Redetermination of the low temperature polymorph of Li_2MnSiO_4 from single crystal X-ray data. Acta Crystallographica, Section E: Structure Reports, (2012), 68, 69.

9 Islam, M. S.; Dominko, R.; Masquelier, C.; Sirisopanaporn, C.; Armstrong, A.R.; Bruce, P.G. Silicate cathodes for lithium batteries: alternatives to phosphates?. Journal of Materials Chemistry, (2011), 21, 9811.

10 West A.R.; Glasser F.P., Preparation and crystal chemistry of some tetrahedral Li_3PO_4-type compounds. Journal of Solid State Chemistry, (1972), 4, 20.

11 West A.R. Crystal chemistry of some tetrahedral oxides. Zeitschrift für Kristallographie, (1975), 141, 422.

12 Duncan H.; Kondamreddy A.; Mercier P.H.J.; Le Page Y.; Abu Lebdeh Y.; Couillard M.; Whitfield P.S.; Davidson I.J. Novel Pn polymorph for Li_2MnSiO_4 and its electrochemical activity as a cathode material in Li-ion batteries. Chemistry of Materials, (2011), 23, 5446.

13 Politaev, V. V.; Petrenko, A. A.; Nalbandyan, V. B.; Medvedev, B. S.; Shvetsova, E. S. Crystal structure, phase relations and electrochemical properties of monoclinic Li_2MnSiO_4. Journal of Solid State Chemistry, (2007), 180, 1045.

14 Gummow, R. J.; Han, G.H.; Sharma, N.; He, Y. Li_2MnSiO_4 cathodes modified by phosphorous substitution and the structural consequences. Solid State Ionics. (2014), 259, 29.

15 Armstrong, A.R.; Sirisopanaporn, C.; Adamson, P.; Billaud, J.; Dominko, R.; Masquelier, C.; Bruce, P.G. Polymorphism in Li_2MSiO_4 (M = Fe, Mn): A Variable Temperature Diffraction Study. Zeitschrift für anorganische und allgemeine Chemie, (2014), 640, 1043.

16 Ramar, V.; Balaya, P. The effect of polymorphism on the lithium storage performance of Li_2MnSiO_4. Journal of Power Sources, (2016), 306, 552.

17 Aravindan, V.; Karthikeyan, K.; Kang, K. S.; Yoon, W. S.; Kim, W. S.; Lee, Y. S. Influence of carbon towards improved lithium storage properties of Li_2MnSiO_4 cathodes. Journal of Materials Chemistry, (2011), 21, 2470.

18 Choi, J.J.; Kim, S.; Im, W.B.; Chang, W.Y.; Cho, B.W.; Kim, J.H.; Choi, H.L.; Chung, K.Y. Synthesis of nanostructured Li_2MnSiO_4/C using a microwave assisted sol–gel process with water as a base solvent. Journal of Electroceramics, (2013), 31, 176.

19 Wang, M.; Yang, M.; Ma, L.Q.; Shen, X.D. The high capacity and excellent rate capability of Ti-doped Li_2MnSiO_4 as a cathode material for Li-ion batteries. RSC Advances, (2015), 5, 1612.

20 Tranqui D.; Shannon, R.D.; Chen H.Y.; Iijima S.; Baur W.H. Crystal structure of ordered Li_4SiO_4. Acta Crystallographica, (1979), B35, 2479.

21 West A.R.; Glasser, F.P. Crystallisation of lithium zinc silicates, Part I Phase equilibria in the system Li_4SiO_4-Zn_2SiO_4. Journal of Materials Science, (1970), 5, 557.

22 West A.R.; Glasser F.P., Crystallisation of lithium magnesium zinc silicates. Journal of Materials Science, (1971), 6, 1100.

23 Fleischmann S.; Mancini M.; Axmann P.; Golla-Schindler U.; Kaiser U.; Wohlfahrt-Mehrens M. Insights into the impact of impurities and non-stoichiometric effects on the electrochemical performance of Li_2MnSiO_4. ChemSusChem, (2016), 9, 2982.

24 Hong H. Y-P. Crystal structure and ionic conductivity of $Li_{14}Zn(GeO_4)_4$ and other new Li^+ superionic conductors. Materials Research Bulletin, (1978), 13, 117.

25 Hannon A.C. Results on disordered materials from the GEneral Materials diffractometer, GEM, at ISIS. Nuclear Instruments and Methods in Physics Research Section A, (2005), 551, 88.

26 Toby B.H. EXPGUI, a graphical user interface for GSAS. Journal of Applied Crystallography, (2001), 34, 210.

27 Bruce P.G.; West A.R. Phase diagram of the LISICON solid electrolyte system, Li_4GeO_4-Zn_2GeO_4. Materials Research Bulletin, (1980), 15, 379.

28 Abrahams I.; Bruce P.G.; West A.R.; David W.I.F, Structure determination of lisicon solid solutions by powder neutron diffraction. Journal of Solid State Chemistry, (1988), 75, 390.

[9 Sears V. F. Neutron scattering lengths and cross sections. Neutron News, (1992), 3, 26.

30 Adv. Energy Mat., (2017), **7,** 1601043

Captions of figures and tables:

Figure 1. The four different polymorphs of Li_2MnSiO_4: (*a*) *Pmn*2_1 [8], (*b*) *Pn* [12], (*c*) *P*2_1/*n* [13] and (*d*) *Pmnb* [14]. Grey, green and blue tetrahedra represent LiO_4, MnO_4 and SiO_4 units, respectively. Oxygen anions are shown as red spheres.

Figure 2. XRD patterns of $Li_{2+2x}Mn_{1-x}SiO_4$ for x from 0 to 1. The samples were slow cooled from 800 ºC.

Figure 3. XRD patterns of $Li_{2+2x}Mn_{1-x}SiO_4$ for x from -0.1 to 1. The samples were quenched from 1000 ºC.

Figure 4. Variation of (*a*-*c*) the lattice parameters *a*, *b* and *c* and (*d*) the unit cell volume, V, of $Li_{2+2x}Mn_{1-x}SiO_4$ with composition x. The intersections of the pairs of

narrow dashed lines are used to estimate the position of the solid solution limit (shown as the thicker, vertical dashed line).

Figure 5. Experimental data points (blue), calculated profile (red) and difference profile (black) illustrating the quality of the Rietveld fit to the (*a*) NPD and (*b*) XRD data of $Li_3Mn_{0.5}SiO_4$. The markers along the top of each figure denote the positions of the reflections allowed by *Pnma* symmetry.

Figure 6. The bond distances for (*a*) the tetrahedrally co-ordinated Li1/Mn1 and Li2/Mn2 positions and (*b*) the octahedrally co-ordinated Li3 and Li4 sites.

Figure 7. The polyhedral structure of $Li_3Mn_{0.5}SiO_4$. The grey tetrahedra represent $(Li1/Mn1)O_4$ and $(Li2/Mn2)O_4$ units, whilst the dark blue tetrahedra are SiO_4. Yellow and cyan spheres show the Li3 and Li4 sites, respectively. Red and black spheres indicate the alternating distorted oxygen *hcp* layers; (*a*) [010] projection and (*b*) [001] projection, showing two *hcp* layers and the associated tetrahedra between the oxygen layers.

Figure 8. Impedance complex plane plots of (*a*) Z* and spectroscopic plots of (*b*) C', (*c*) Y' and (*d*) –Z'' and M'' for $Li_3Mn_{0.5}SiO_4$ at the temperatures indicated.

Figure 9. Arrhenius plots of (*a*) Li_4SiO_4, Li_2MnSiO_4 and $Li_3Mn_{0.5}SiO_4$ and (*b*) quenched $Li_{3.5}Mn_{0.25}SiO_4$ and slow cooled $Li_{3.5}Mn_{0.25}SiO_4$. In each case, the activation energies, E_a, derived from the data are shown.

Table 1. Phases present in samples of $Li_{2+2x}Mn_{1-x}SiO_4$ for different compositions, x, and heat treatments, as determined by XRD. The abbreviations are *LMS*: Li_2MnSiO_4; M_2S: Mn_2SiO_4; L_3MS_2: $Li_3Mn_{0.5}SiO_4$ and L_2S: Li_4SiO_4. *ss* refers to a solid solution

and Low L_2S *ss* is an L_2S *ss* phase showing extra superlattice reflections in its XRD pattern.

Table 2. Indexing results of $Li_3Mn_{0.5}SiO_4$ using XRD data. The observed reflections are consistent with an orthorhombic unit cell of dimensions a = 10.722(3)Å, b = 6.239(2)Å and c = 5.052(3)Å. The hkl values of the observed reflections are consistent with the reflection conditions of space group *Pnma* symmetry (0kl, k+l=2n; hk0, h=2n; h00, h=2n; 0k0, k=2n and 00l, l=2n).

Table 3. Indexing results of a quenched of sample L_2S *ss* of composition x=0.3, $Li_{3.4}Mn_{0.3}SiO_4$, using XRD data. The observed reflections are consistent with a monoclinic unit cell with a = 5.328(4)Å, b = 5.137(3)Å, c = 6.145(4)Å and β= 90.3(1)°.

Table 4. Refined structural parameters of $Li_3Mn_{0.5}SiO_4$ obtained by simultaneous fitting of the NPD and XRD data. The positional parameters shown in italics are those for an idealised structure based on cations occupying the centres of their polyhedra in a perfect *hcp* array of anions. The u_{iso} values are the isotropic thermal vibration parameters. The value of the overall goodness-of-fit parameter, χ^2, is given in the lower panel, together with the individual weighted profile R-factors, R_{wp}, and profile R-factors, R_p.

Table 5. Bond lengths within the cation-centred polyhedra of $Li_3Mn_{0.5}SiO_4$, derived from the structural parameters given in table 4.

Table 6. Bond angles within the cation-centred tetrahedra of $Li_3Mn_{0.5}SiO_4$, derived from the structural parameters given in table 4.

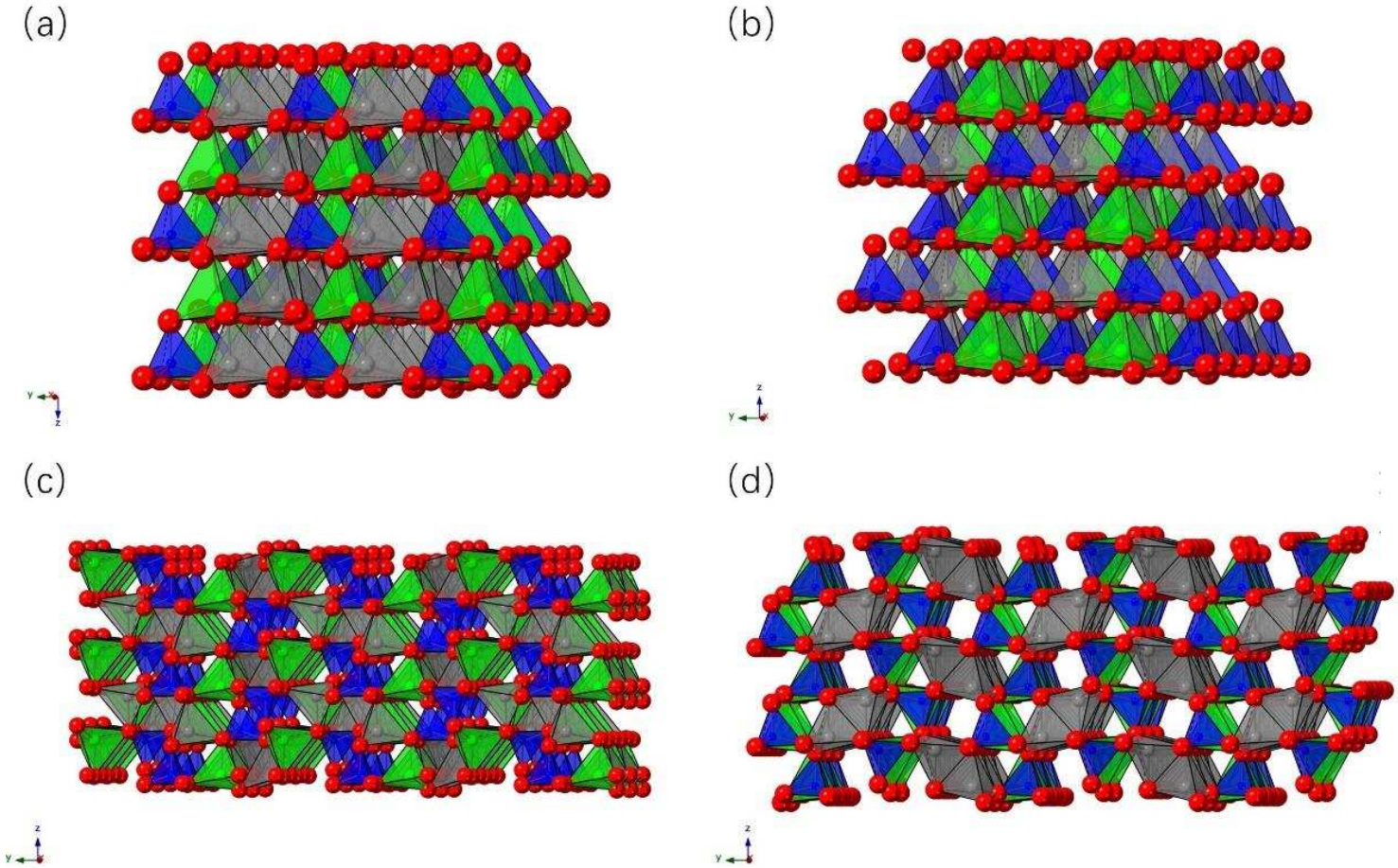

Figure 1

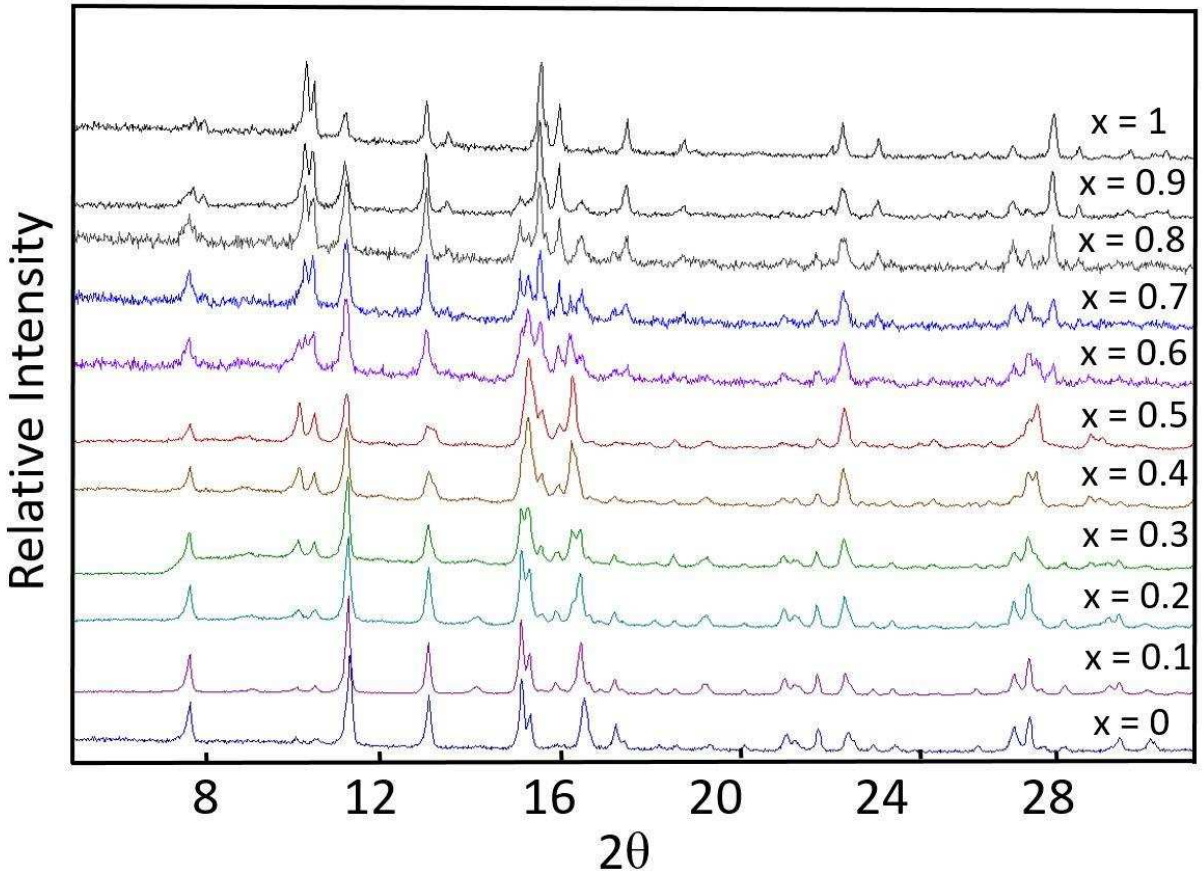
Relative Intensity
x = 1
x = 0.9
x = 0.8
x = 0.7
x = 0.6
x = 0.5
x = 0.4
x = 0.3
x = 0.2
x = 0.1
x = 0
8
12
16
20
24
28
2θ

Figure 2

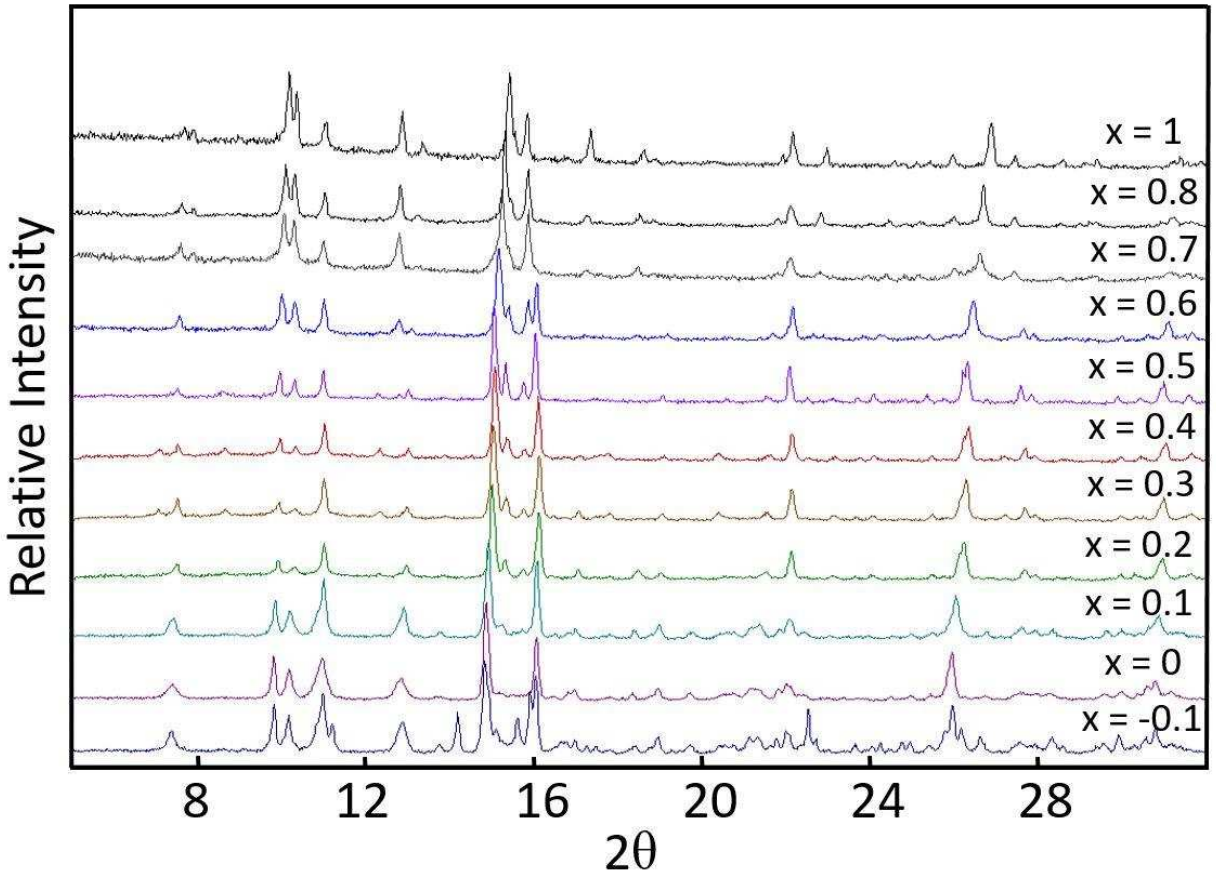
Relative Intensity
x = 1
x = 0.8
x = 0.7
x = 0.6
x = 0.5
x = 0.4
x = 0.3
x = 0.2
x = 0.1
x = 0
x = -0.1
8
12
16
20
24
28
2θ

Figure 3

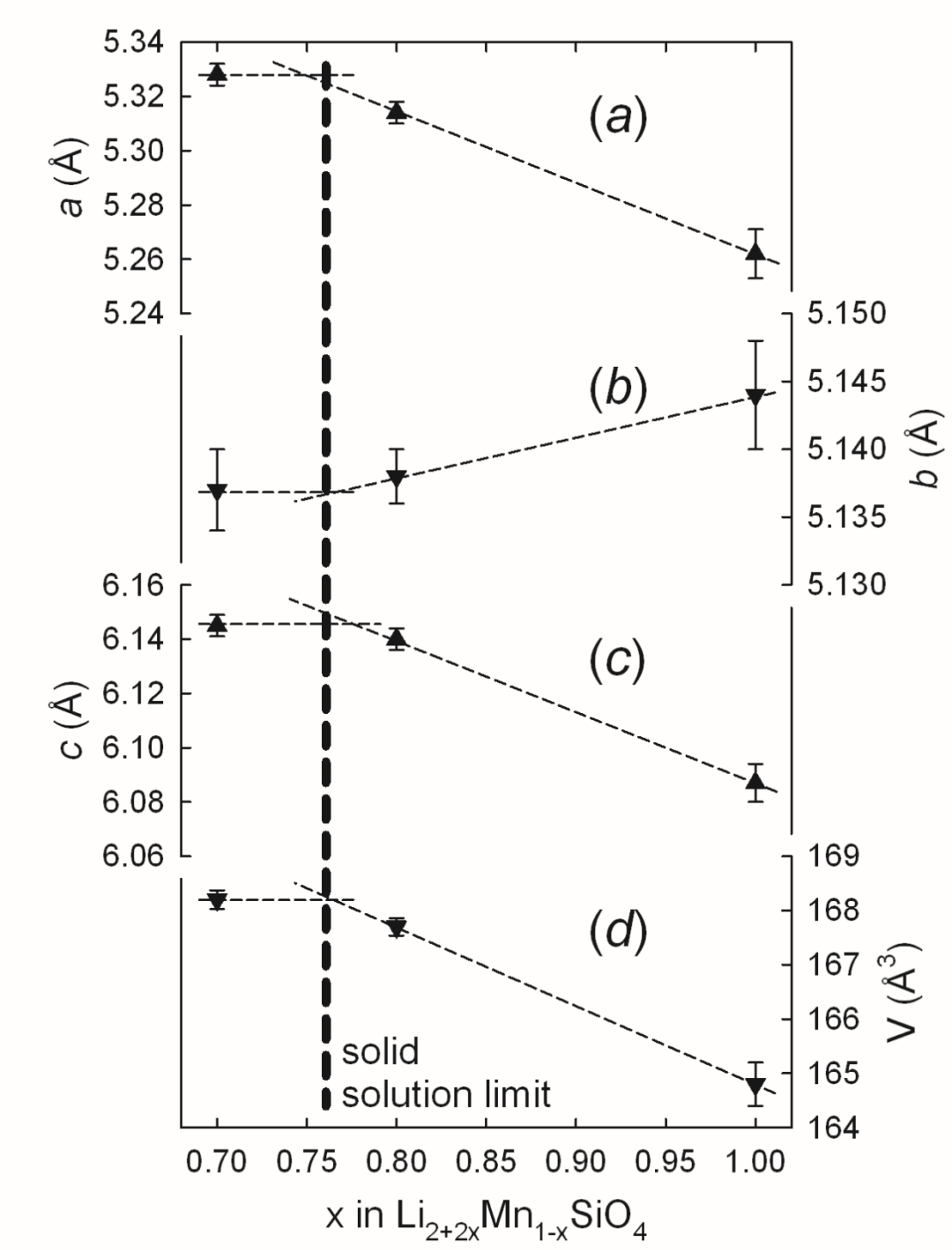
5.34
5.32
5.30
5.28
5.26
5.24
a (Å)
(a)
5.150
5.145
5.140
5.135
5.130
b (Å)
(b)
6.16
6.14
6.12
6.10
6.08
6.06
c (Å)
(c)
169
168
167
166
165
164
V (Å3)
(d)
solid
solution limit
0.70
0.75
0.80
0.85
0.90
0.95
1.00
x in Li2+2xMn1-xSiO4

Figure 4

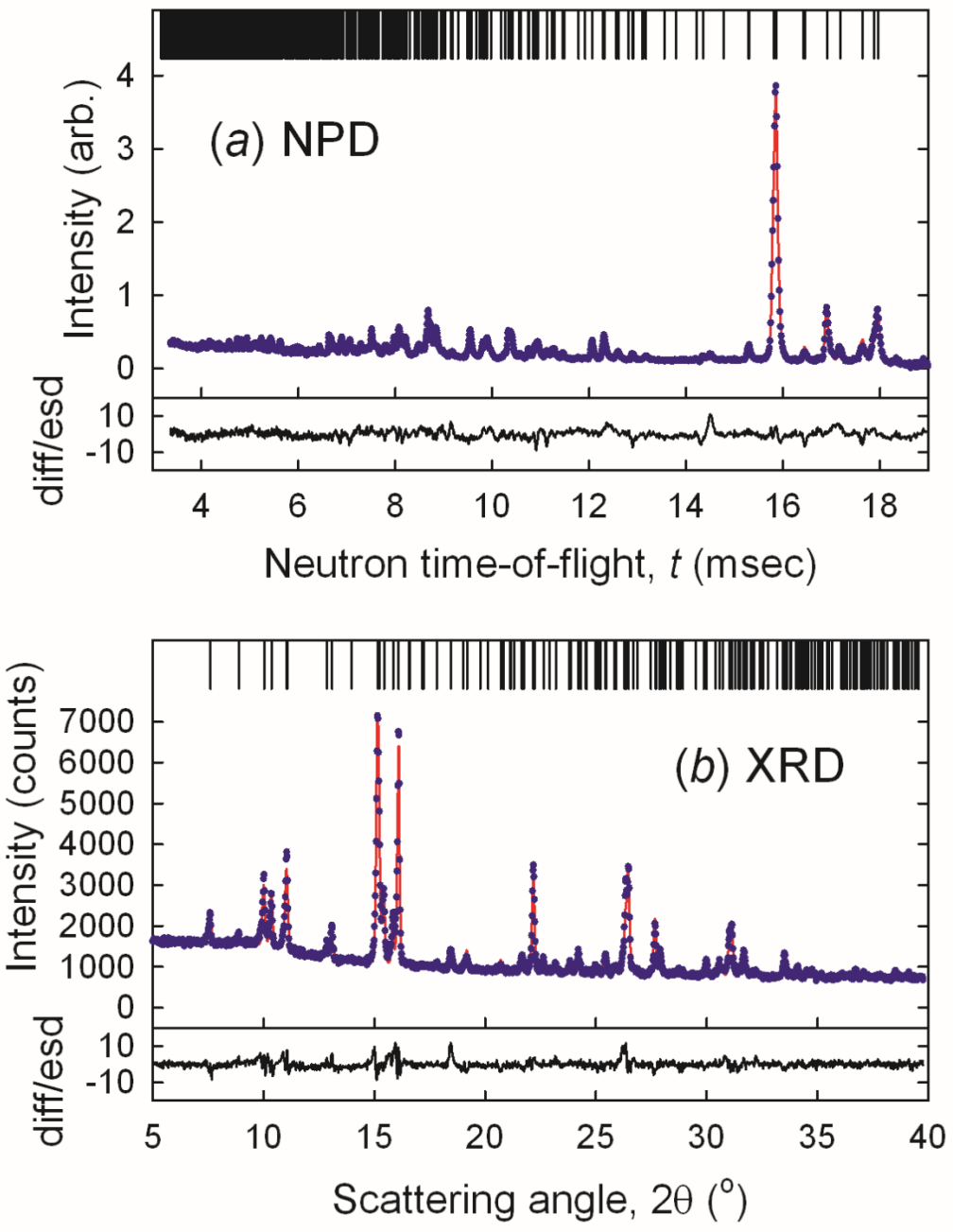
(a) NPD
Intensity (arb.)
diff/esd
Neutron time-of-flight, t (msec)
(b) XRD
Intensity (counts)
diff/esd
Scattering angle, 2θ (°)

Figure 5

(*a*)

(*b*)

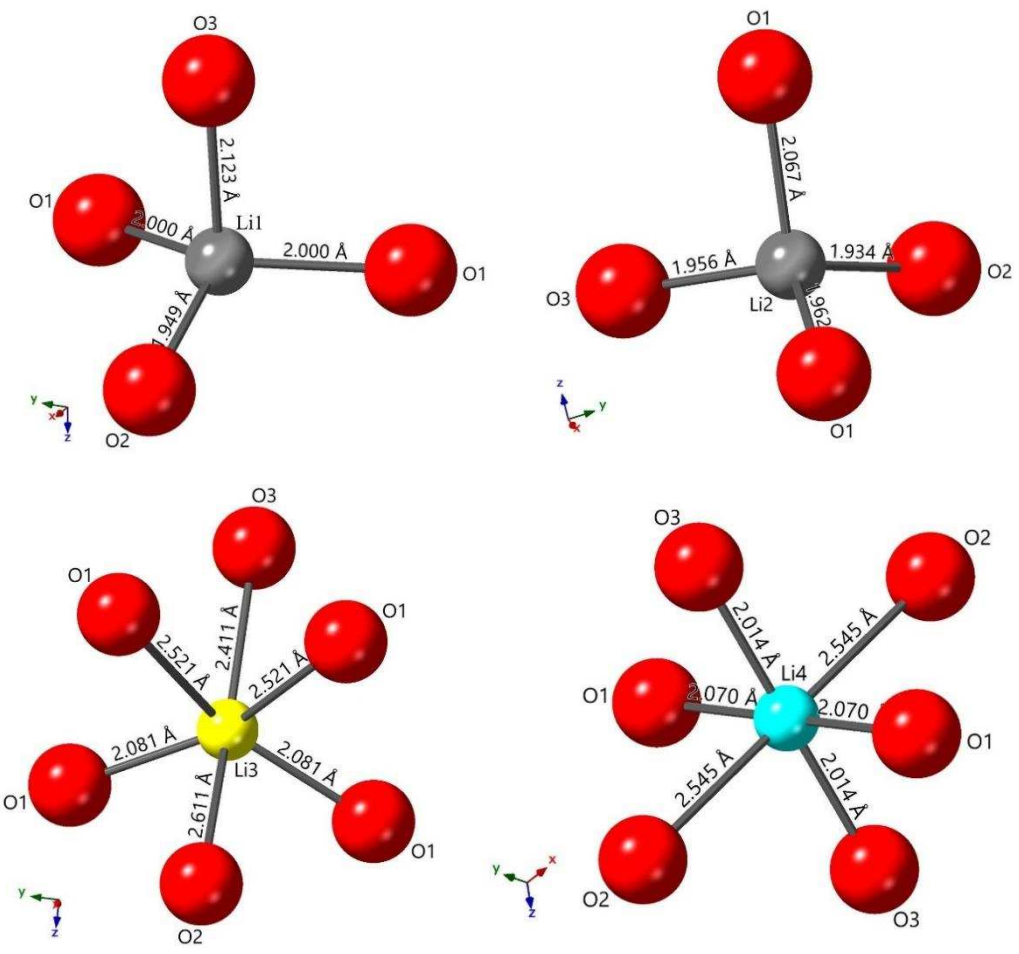
O3
2.123 Å
O1
2.000 Å
Li1
2.000 Å
O1
1.949 Å
O2
O1
2.067 Å
1.956 Å
1.934 Å
O2
O3
Li2
1.962
O1
O3
O1
2.521 Å
2.411 Å
2.521 Å
O1
2.081 Å
Li3
2.081 Å
O1
2.611 Å
O2
O3
O2
2.014 Å
2.545 Å
O1
2.070 Å
Li4
2.070
O1
2.545 Å
2.014 Å
O2
O3

Figure 6

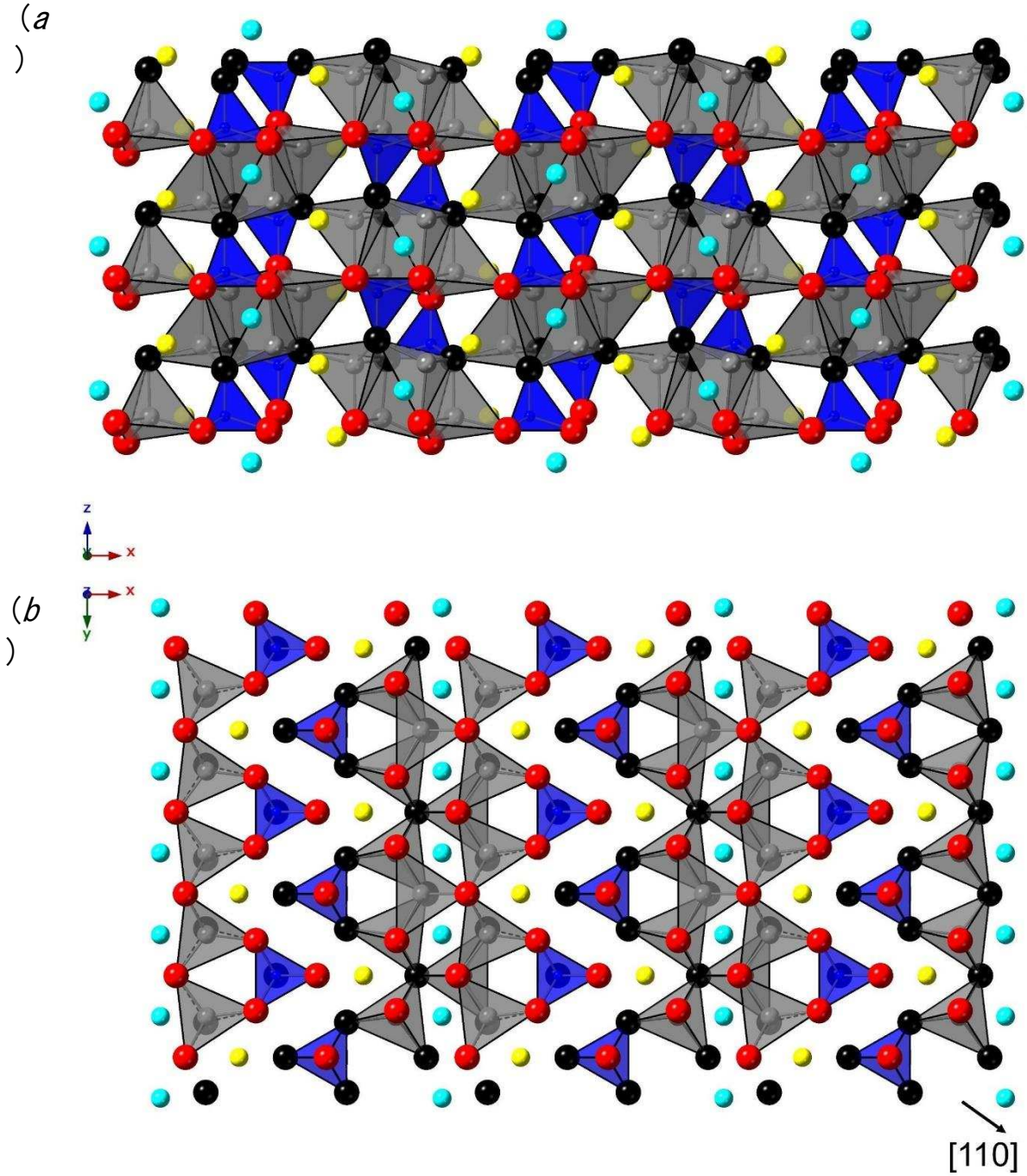

Figure 7

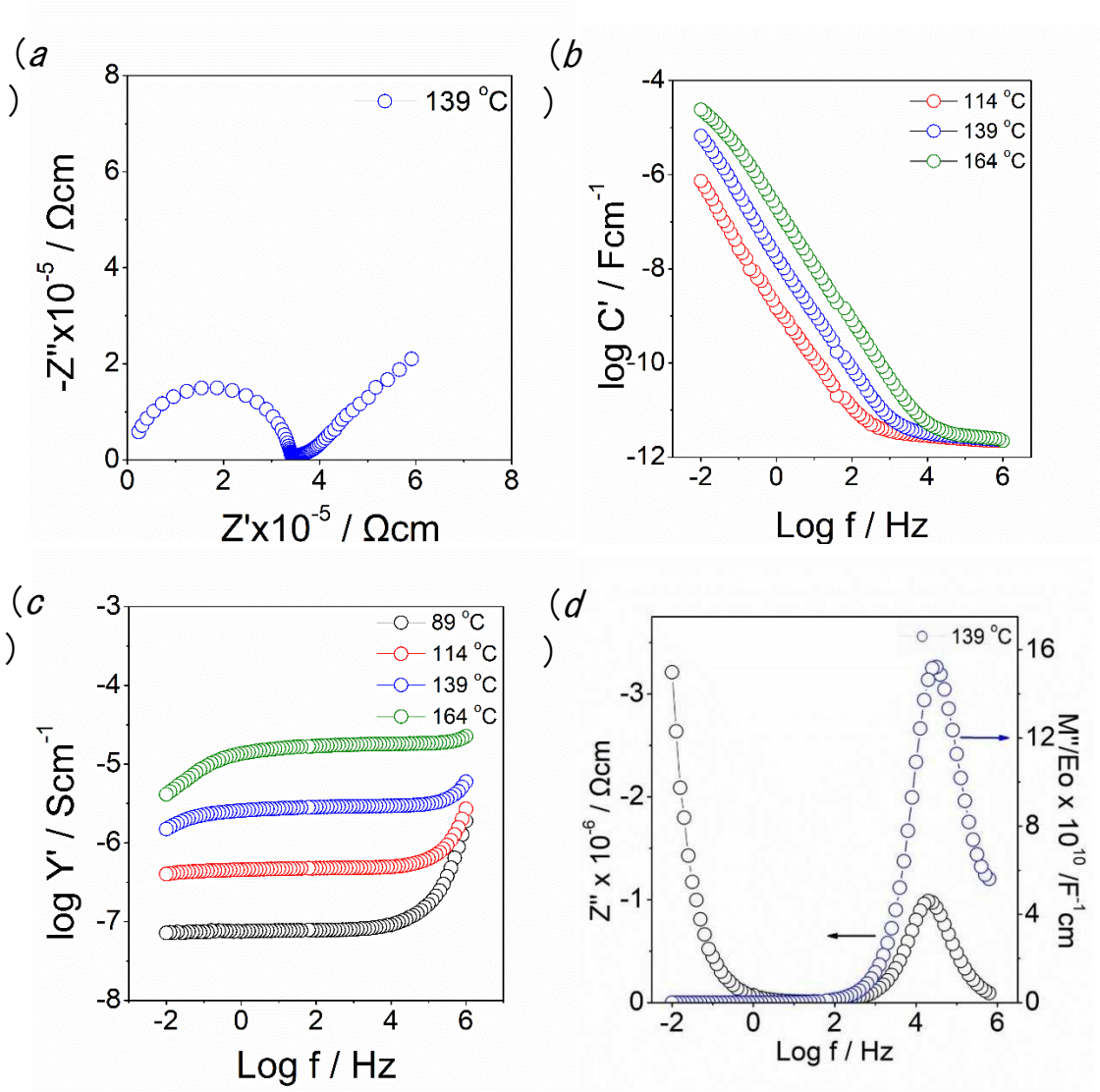
(a)
139 °C
-Z''x10^-5 / Ωcm
Z'x10^-5 / Ωcm
(b)
114 °C
139 °C
164 °C
log C' / Fcm^-1
Log f / Hz
(c)
89 °C
114 °C
139 °C
164 °C
log Y' / Scm^-1
Log f / Hz
(d)
139 °C
Z'' x 10^-6 / Ωcm
M''/Eo x 10^10 /F^-1cm
Log f / Hz

Figure 8

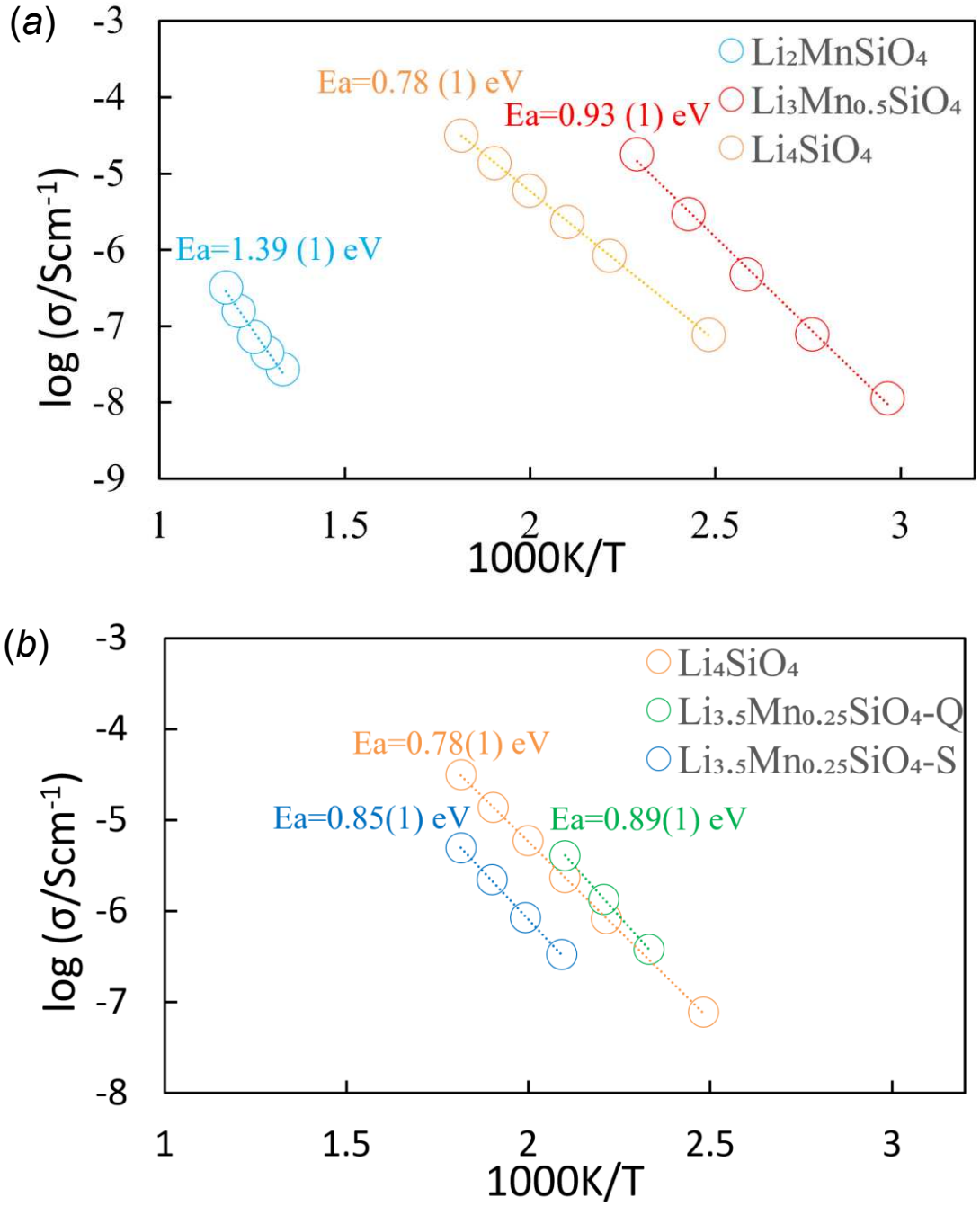
(a)
Li2MnSiO4
Li3Mn0.5SiO4
Li4SiO4
Ea=0.78 (1) eV
Ea=0.93 (1) eV
Ea=1.39 (1) eV
log (σ/Scm-1)
1000K/T
(b)
Li4SiO4
Li3.5Mn0.25SiO4-Q
Li3.5Mn0.25SiO4-S
Ea=0.78(1) eV
Ea=0.85(1) eV
Ea=0.89(1) eV
log (σ/Scm-1)
1000K/T

Figure 9

Composition	Detected phases : slow cooled from 800 ºC	Detected phases : quenched from 1000 ºC
x = -0.1: $Li_{1.8}Mn_{1.1}SiO_4$	β-*LMS* and M_2S	γ-*LMS* and M_2S
x = 0: Li_2MnSiO_4	β-*LMS*	γ-*LMS*
x = 0.1: $Li_{2.2}Mn_{0.9}SiO_4$	β-*LMS*	γ-*LMS* and L_3MS_2
x = 0.2: $Li_{2.4}Mn_{0.8}SiO_4$	β-*LMS* and L_3MS_2	γ-*LMS* and L_3MS_2
x = 0.3: $Li_{2.6}Mn_{0.7}SiO_4$	β-*LMS* and L_3MS_2	γ-*LMS* and L_3MS_2
x = 0.4: $Li_{2.8}Mn_{0.6}SiO_4$	β-*LMS* and L_3MS_2	γ-*LMS* and L_3MS_2
x = 0.5: $Li_3Mn_{0.5}SiO_4$	L_3MS_2	L_3MS_2
x = 0.6: $Li_{3.2}Mn_{0.4}SiO_4$	Low L_2S *ss* and L_3MS_2	L_2S *ss* and L_3MS_2
x = 0.7: $Li_{3.4}Mn_{0.3}SiO_4$	Low L_2S *ss* and L_3MS_2	L_2S *ss* and L_3MS_2
x = 0.8: $Li_{3.6}Mn_{0.2}SiO_4$	Low L_2S *ss*	L_2S *ss*
x = 0.9: $Li_{3.8}Mn_{0.1}SiO_4$	Low L_2S *ss*	L_2S *ss*
x = 1: Li_4SiO_4	L_2S	L_2S

Table 1

n	*h*	*k*	*l*	Intensity	d_{obs} (Å)	Δ2θ(obs-calc)
1	2	0	0	33	5.3509	0.0144
2	1	0	1	25	4.5762	-0.0114
3	2	1	0	47	4.0609	0.0127
4	0	1	1	39	3.9231	0.0086
5	2	0	1	54	3.6726	0.0128
6	2	1	1	23	3.1601	0.0309
7	0	2	0	27	3.1216	-0.0092
8	2	2	0	100	2.6935	0.0154
9	3	1	1	42	2.6431	-0.0003
10	1	2	1	30	2.5759	0.0039
11	0	0	2	73	2.5239	0.0151
12	1	1	2	15	2.2832	0.0345
	2	0	2			0.0155
13	4	1	1	16	2.2178	-0.0331
14	3	2	1	18	2.1317	-0.0073
15	5	0	1	15	1.9732	0.0079
16	1	3	1	18	1.8927	0.0020
17	2	2	2	43	1.8431	0.0047
18	2	3	1	17	1.8105	-0.0040
19	4	1	2	14	1.7642	-0.0104
20	6	1	0	16	1.7172	0.0101
21	3	3	1	19	1.6931	0.0064
22	4	3	0	14	1.6430	0.0010
23	1	1	3	17	1.6087	-0.0187
	2	0	3			-0.0323
24	0	4	0	37	1.5597	0.0009
25	6	2	0	49	1.5507	-0.0023
26	3	0	3	13	1.5235	-0.0015
27	1	2	3	19	1.4683	-0.0063
28	2	2	3	14	1.4280	0.0075
	7	1	1			-0.0211
29	3	2	3	16	1.3686	0.0073
30	4	4	0	16	1.3488	-0.0154
31	6	2	2	31	1.3218	-0.0066
32	1	3	3	17	1.2987	0.0119
33	1	1	4	19	1.2295	0.0073
	2	0	4			-0.0032

Table 2

n	*h*	*k*	*l*	Intensity	d_{obs} (Å)	Δ2θ(obs-calc)
1	1	0	0	46	5.3436	-0.0225
2	0	1	0	40	5.1309	0.0093
3	-1	0	1	78	4.0360	0.0023
4	0	1	1	72	3.9455	-0.0110
5	1	1	0	50	3.6965	0.0046
6	-1	1	1	56	3.1795	-0.0220
7	-1	0	2	100	2.6706	-0.0132
8	0	2	0	80	2.5678	0.0039
9	1	1	2	23	2.3581	0.0044
10	-2	1	1	25	2.2094	0.0115
11	-1	2	2	35	1.8504	0.0007
	2	2	0			-0.0169
12	-1	1	3	20	1.7941	0.0103
13	-1	3	1	25	1.5764	-0.0011
	1	3	1			-0.0239
14	-3	0	2	40	1.5411	0.0048
15	0	3	2	21	1.4959	-0.0033

Table 3

Atom	*x*	*y*	*z*	Mult.	Occupancy	u_{iso}×100 (Å^2)
Si1	0.4121(4)	$^1/_4$	0.3222(6)	4	1	0.55(7)
	0.4167	*$^1/_4$*	*0.3750*			
O1	0.3394(2)	0.0360(3)	0.2224(4)	8	1	1.15(6)
	0.3333	*0.0*	*0.25*			
O2	0.0892(3)	$^3/_4$	0.1505(5)	4	1	1.03(6)
	0.0833	*$^3/_4$*	*0.25*			
O3	0.0554(3)	$^1/_4$	0.2767(5)	4	1	0.94(8)
	0.0833	*$^1/_4$*	*0.25*			
Li1	0.4231(8)	$^3/_4$	0.190(1)	4	0.815(6)	2.1(2)
	0.4167	*$^3/_4$*	*0.125*			
Mn1	=x_{Li1}	=y_{Li1}	=z_{Li1}	4	0.185(6)	=u_{Li1}
Li2	0.1632(6)	-0.0013(9)	0.317(1)	8	0.877(4)	1.9(1)
	0.1667	*0.0*	*0.375*			
Mn2	=x_{Li2}	=y_{Li2}	=z_{Li2}	8	0.123(4)	=u_{Li2}
Li3	0.202(3)	$^1/_4$	-0.084(7)	4	0.16(4)	10(2)
	0.25	*$^1/_4$*	*0.0*			
Li4	$^1/_2$	0	0	4	0.16(3)	8(2)
	$^1/_2$	*0*	*0*			

Space group : *Pnma*
a = 10.7193(4)Å, b = 6.2272(3)Å, c = 5.0695(2)Å
(ideal *hcp* : a = 10.752Å, b = 6.208Å, c = 5.069Å)
χ^2 = 4.680
R_{wp} = 4.75%, R_p = 6.10% for NPD
R_{wp} = 6.51%, R_p = 4.62% for XRD
Refined composition : $Li_{2.89(8)}Mn_{0.43(4)}SiO_4$

Table 4

Bond	Length (Å)
Si-O3	1.615(5)
Si-O1 (×2)	1.624(3)
Si-O2	1.664(4)
Li1/Mn1-O2	1.949(8)
Li1/Mn1-O1 (×2)	2.000(4)
Li1/Mn1-O3	2.123(8)
Li2/Mn2-O1	1.934(6)
Li2/Mn2-O2	1.956(6)
Li2/Mn2-O3	1.962(7)
Li2/Mn2-O1	2.067(5)
Li3-O1 (×2)	2.08(2)
Li3-O3	2.41(3)
Li3-O1 (×2)	2.52(3)
Li3-O2	2.61(3)
Li4-O3 (×2)	2.014(2)
Li4-O1 (×2)	2.070(2)
Li4-O2 (×2)	2.545(2)

Table 5

Bond angle	Angle (°)
O1-Si-O2 (×2)	107.9(2)
O2-Si-O3	108.6(3)
O1-Si-O3 (×2)	111.1(1)
O1-Si-O1	110.2(2)
O1-Li1/Mn1-O3 (×2)	97.5(2)
O2-Li1/Mn1-O3	108.2(4)
O1-Li1/Mn1-O2 (×2)	112.0(2)
O1-Li1/Mn1-O1	125.8(4)
O1-Li2/Mn2-O3	100.3(3)
O1-Li2/Mn2-O1	105.5(3)
O1-Li2/Mn2-O2	110.1(3)
O2-Li2/Mn2-O3	110.7(4)
O1-Li2/Mn2-O2	112.6(3)
O1-Li2/Mn2-O3	116.7(3)

Table 6